Supporting Information

Welsher et al. 10.1073/pnas.1014501108

SI Text

Principal Component Analysis (PCA). PCA is a common statistical processing method for compressing high-dimensional data into a lower-dimensional form by choosing only the highest variance components of the dataset (1). PCA is performed on groups of images by considering each pixel to be an observation that varies over the variable time. The data is N dimensional, where N is the number of time points in the series of images. The $p \times N$ matrix (where p is the number of pixels in the image) is converted to a covariance matrix by multiplying by its transpose and subtracting the time-averaged mean values of each pixel. This covariance matrix is then diagonalized to find eigenvalues (variances) and eigenvectors (components). The eigenvectors point in the direction of greatest variance for a given component. The first component has the highest variance, similar to a weighted mean over all the images. The second component is in the direction of next highest variance that is orthogonal to the first component (Fig. S3). The third component (Fig. S3) is orthogonal to both the first and second components, and so on. As a linear combination of the initial images, each principal component is made up of positive and negative pixels (Fig. S3), both of which indicate high variance but with different behavior along that particular component axis.

Detailed Methods. ***Preparation of biocompatible single-walled carbon nanotube (SWNT) fluorophores with high relative quantum yield.*** The preparation of brightly fluorescent exchanged-SWNTs with high biocompatibility can be found in detail in ref. 2 by using a surfactant exchange method to minimize damage to SWNTs. Briefly, raw high-pressure carbon monoxide synthesized SWNTs (Unidym) were suspended in 1 wt% sodium cholate hydrate in water by 1 h of bath sonication. This suspension was ultracentrifuged at $300{,}000 \times g$ to remove bundles and other large aggregates. The supernatant was retained and 1 mg/mL of DSPE-mPEG (1,2-distearoyl-*sn*-glycero-3-phosphoethanolamine-N-[methoxy (polyethylene glycol)5000]) (Laysan Bio) was added. The resulting suspension was dialyzed against a 3,500 molecular weight cutoff membrane (Fisher) with a minimum of six water changes and a minimum of 2 h between water changes. As a final step, the suspension was ultracentrifuged again for 1 h at $300{,}000 \times g$ to remove any aggregates. A fluorescence emission spectrum of the resulting SWNTs with DSPE-mPEG coating at 808-nm excitation is shown in Fig. 1*B*. A photoluminescence excitation/emission spectrum of the DSPE-mPEG SWNTs can be found in Fig. S10.

Video-rate imaging in the second near-infrared window (NIR II). Video-rate imaging was performed on a homebuilt setup consisting of a 2D InGaAs array (Princeton Instruments). The geometry of the imaging setup is shown in Fig. 1*a*=*A*. The excitation light was provided by a fiber-coupled 808-nm diode laser (RMPC Lasers). This wavelength was chosen to overlap with the traditional biological transparency window. It should be noted that other excitation/emission combinations are possible further into the NIR II, with larger-diameter nanotubes exhibiting excitation and emission bands beyond 900 and 1500 nm, respectively (3). These wavelengths may have further reduced scattering, but an analysis of these regions is beyond the scope of this work. The light was collimated by a 4.5-mm focal length collimator (ThorLabs) and filtered to remove unwanted radiation in the emission range. The excitation spot was a circle with a diameter of approximately 6 cm. The excitation power at the imaging plane was approximately 5 W, leading to power density of approximately 140 mW/cm^2. Emitted light was passed through an 1,100-nm longpass filter (ThorLabs FEL1100) and focused onto the detector by a lens pair consisting of two NIR achromats (200 and 75 mm; Thorlabs). The 1,100-nm longpass filter was chosen to select the majority of the wavelength emission, while rejecting autofluorescence that may occur near the excitation band. The camera was set to expose continuously, and images were acquired with LabVIEW software at highest possible frame rate. The exposure time for all images shown is 50 ms. There was a 19-ms overhead in the readout, leading to an average time of 69 ms between consecutive frames. Two thousand consecutive frames were collected, leading to a total imaging time of 2 min and 18 s. For imaging, five female athymic nude mice were used, and results shown are representative. The ideal concentration for injection and video-rate imaging was determined to be 200 μL of approximately 500-nM SWNT solution (optical density ~4 at 808 nm) (4). It was observed that higher concentration led to a loss of feature clarity, whereas lower concentration or injection volume led to lower than desired signal to noise.

Mouse handling and injection. Female athymic nude mice were obtained from Harlan Sprague Dawley and were housed at Stanford Research Animal Facility in accordance with Institutional Animal Care and Use Committee protocols. During imaging, mice were anaesthetized by inhalation of 2% isoflurane with oxygen. For SWNT injection, a 30-gauge catheter was inserted into the lateral tail vein, allowing for bolus injection during the first frames of imaging.

Monte Carlo simulation. Simulations were performed following the procedure from ref. 5 using MATLAB. The simulation considered photon packets of starting weight W emitted from a point source embedded in a turbid medium. The emission angle was limited to $\pm 30°$ to conserve computing power. Simulation of a point source with limited emission angle could give quantitatively different results as obtained in our phantom experiments, but the qualitative trends seem to agree. The photon packet traveled a distance of $d = -\ln(\mathrm{RAND})/\mu_s'$ before encountering a scattering event. Scattering was considered to be isotropic with a uniform angular distribution. After each scattering event, the weight of each packet was reduced by a factor of $\exp(-\mu_a \cdot d)$. Upon reaching the tissue/air interface, the packet underwent refraction according to Snell's Law. The displacement and direction of the packet at the interface was then projected onto the image space using ray matrices derived from the actual experimental setup. The imaged light packets were binned into 10-μm steps over a 2-mm by 2-mm area, and the resulting images were plotted. The values for μ_a for water (0.098 ± 0.002 mm^{-1} at 800 nm and 0.140 ± 0.02 mm^{-1} at 1,300 nm) were measured using a UV-Vis-NIR (Varian Cary 6000i). The value of μ_s' for Intralipid® was obtained from the literature following the relation $\mu_s' = 16 \cdot \lambda^{-2.4}$, where λ is the wavelength in microns (6). This resulted in μ_s' values of 2.73 and 0.852 at 800 and 1300 nm, respectively.

1. Lay DC (2003) *Linear Algebra and Its Applications* (Addison Wesley, Boston).
2. Welsher K, et al. (2009) A route to brightly fluorescent carbon nanotubes for near-infrared imaging in mice. *Nat Nanotechnol* 4:773–780.

3. Bachilo SM, et al. (2002) Structure-assigned optical spectra of single-walled carbon nanotubes. *Science* 298:2361–2366.
4. Kam NWS, O'Connell M, Wisdom JA, Dai H (2005) Carbon nanotubes as multifunctional biological transporters and near-infrared agents for selective cancer cell destruction. *Proc Natl Acad Sci USA* 102:11600–11605.
5. Splinter R, Hooper BA (2007) *An Introduction to Biomedical Optics* (Taylor & Francis, New York).
6. Vanstaveren HJ, et al. (1991) Light-scattering in intralipid-10% in the wavelength range of 400–1100 Nm. *Appl Opt* 30:4507–4514.

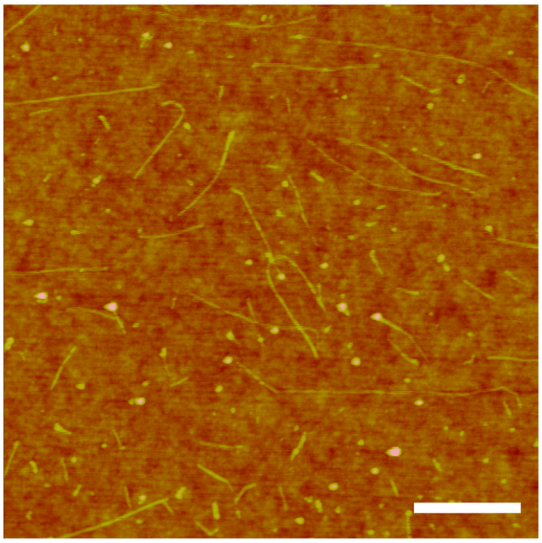

Fig. S1. Atomic force microscopy image of bright, biocompatible SWNTs in DSPE-mPEG deposited on a SiO_2 surface. Length ranges from 200–500 nm with a mean length of approximately 350 nm. Scale bar represents 200 nm (2).

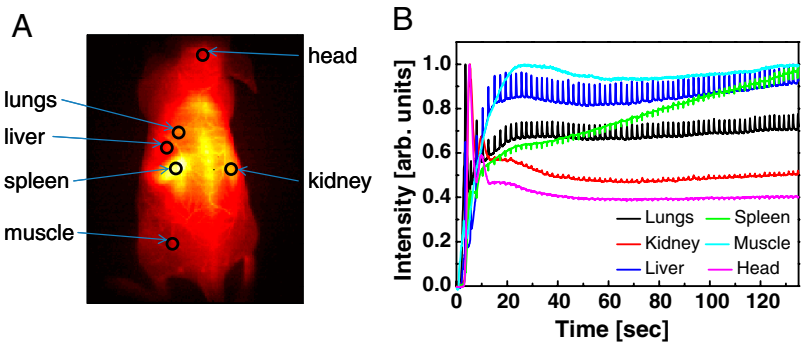

Fig. S2. Region of interest (ROI) time traces. (*A*) Regions used to generate the normalized ROI time traces shown in Fig. 2 *I* and *J*. (*B*) ROI time traces obtained from the regions in *A* without removal of breathing frames.

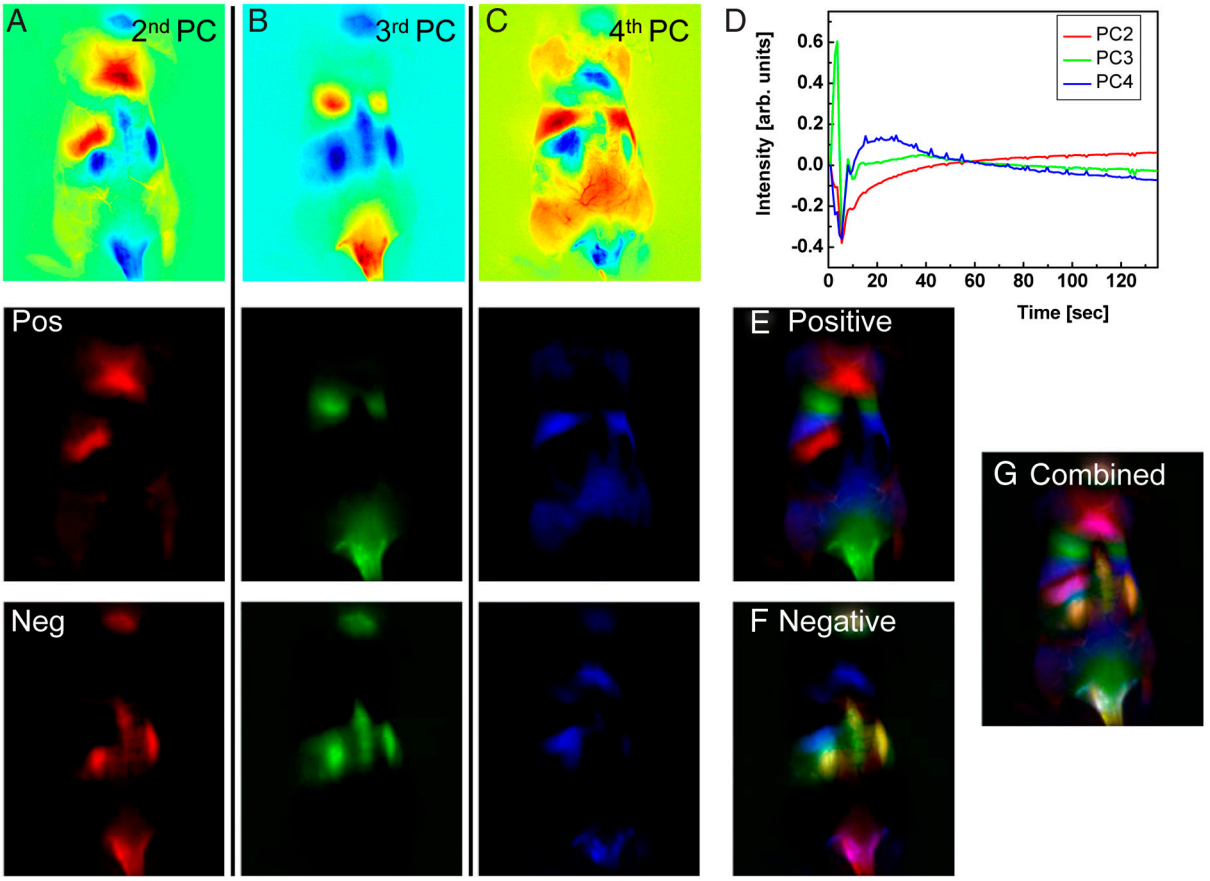

Fig. S3. Building PCA images. Following PCA analysis by MATLAB, the (*A*) second (red), (*B*) third (green), and (*C*) fourth (blue) components are retained. (*D*) The principal component eigenvectors show how each principle component image is composed from the raw time-course images. The *y* axis reports the coefficient used for each *x*-axis time frame to make the linear combination of images for each principal component. (*E*) Positive image overlay. Only the positive pixels are retained by setting the negative pixels to zero. (*F*) For the negative images, the negative pixels are retained and inverted to make the composite image. (*G*) For the combined image, the absolute value of each pixel is plotted in an effort to retain all information.

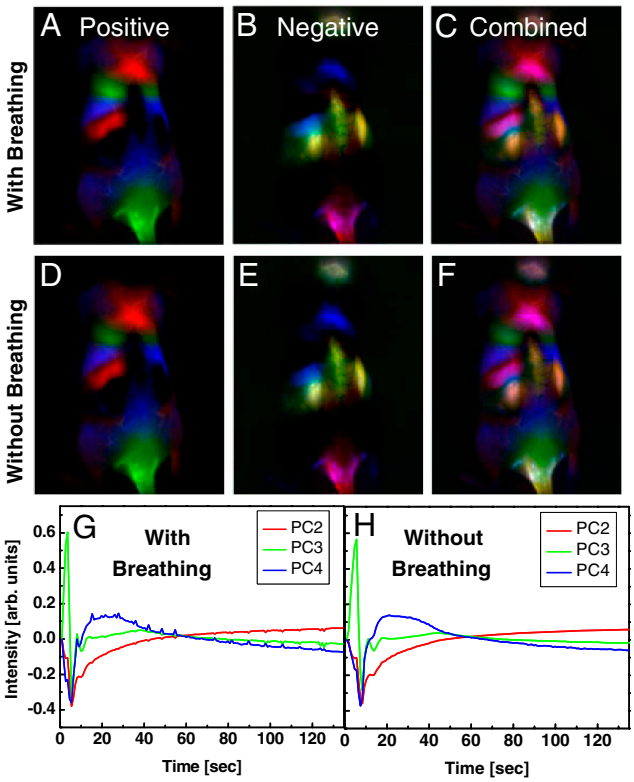

Fig. S4. Effect of breathing movements on PCA. (*A*) Positive pixels, (*B*) negative pixels, and (*C*) a combined overlay obtained by performing PCA on a complete series ("With Breathing") of images as in Figs. 3 and 4. To rule out breathing-related artifacts, frames involving movement of the animal were manually removed and PCA was performed on this edited series of images. The (*D*) positive pixels, (*E*) negative pixels, and (*F*) combined overlay of the "Without Breathing" series shows the same organs resolved in parts *A*–*C*. The similarity confirms that overlapping organs are not artifacts due to breathing motion of the animal. The principal component eigenvectors of the (*G*) "With Breathing" series shows a similar trend to the (*F*) "Without Breathing" series. PCA for each dataset was performed on approximately 150 frames spanning the first approximately 130 s postinjection.

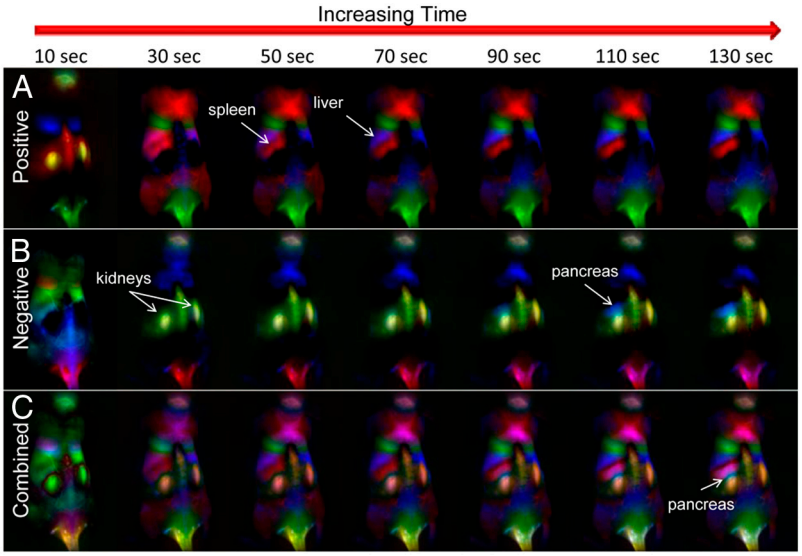

Fig. S5. Time-dependent PCA Iimages. (*A*) Positive-only pixels from time-dependent PCA. The liver and spleen show up at about 50 s and become clearer with increasing time. (*B*) Negative-only pixels from time-dependent PCA. The kidneys appear at 30 s and remain constant throughout the time course. The pancreas appears as a blue feature above the left kidney at 90 s and increases in intensity with increasing time. (*C*) Absolute value of pixels from time-dependent PCA, showing increased clarity of the reticuloendothelial system organs (liver, spleen) with increasing time, as well as the appearance of a spatially distinct pancreas feature at 90 s.

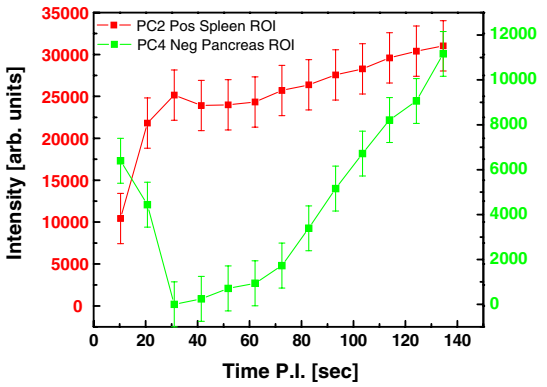

Fig. S6. Time-dependent PCA ROI. ROI time course of spleen and pancreas features from time-dependent PCA, showing different behavior in time. For the red curve, ROIs were drawn over the spleen component in the positive pixels of the second principal component. An average intensity was taken at each time point in the time-course PCA data. The error bars represent the standard deviation of the intensity values in the ROI. The green curve was determined in a similar way, using the pancreas region of the negative pixels of the fourth principal component. The pancreas is not visible before 90 s, whereas the spleen is visible at 30 s. This temporal difference indicates that these two features belong to different organs.

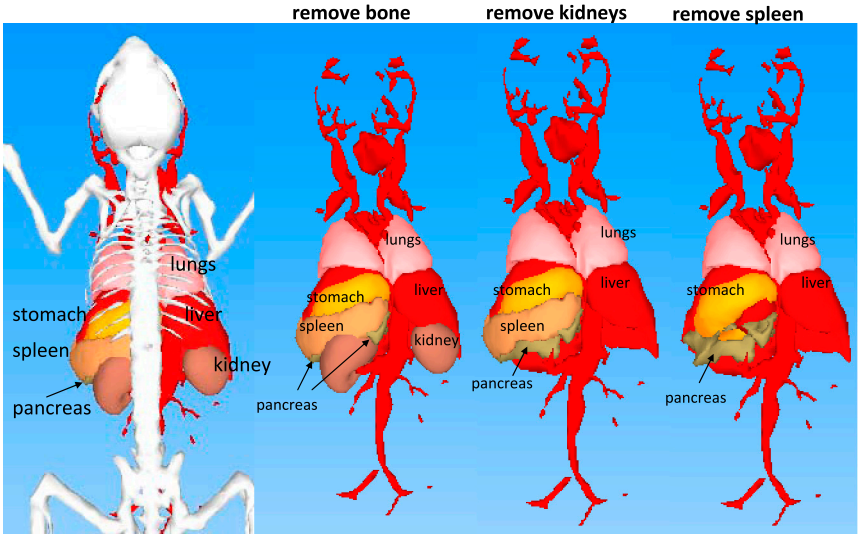

Fig. S7. Pancreas location. Mouse anatomy showing the location of the pancreas, when the bone, kidney, and spleen are successively removed.

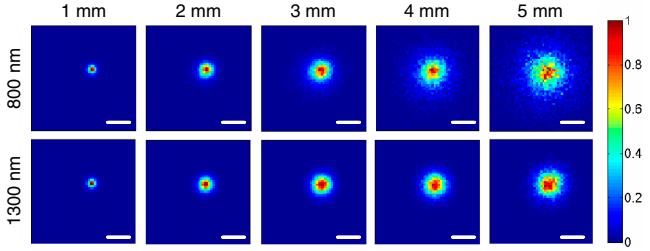

Fig. S8. Monte Carlo simulation. Monte Carlo–generated images (see *Methods* section in main text for details) as a function of emission wavelength and depth for a point source in Intralipid®. The computed image shows a greater spread in the feature size with depth for the 800-nm emitter (top row) compared to the 1,300-nm emitter (bottom row), showing the benefit of imaging in the low albedo NIR II region. Scale bars represent 3 mm.

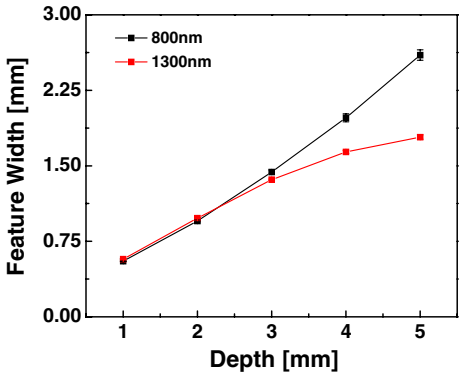

Fig. S9. Monte Carlo simulation feature spreading. Feature width as a function of depth for the NIR I and NIR II, generated from the Monte Carlo simulation of emission from a point source embedded in Intralipid®. The simulation shows a greater loss of feature integrity for the NIR I. Error bars are derived from the uncertainty in the fitting of feature width.

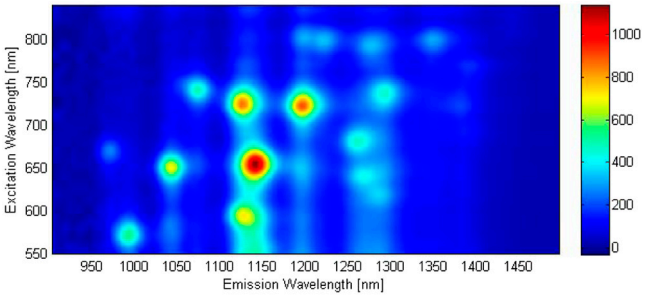

Fig. S10. Fluorescence excitation/emission spectrum. Fluorescence excitation versus emission spectrum of SWNTs suspended in DSPE-mPEG. Although the sample shows SWNT excitation below 800 nm, an 808-nm laser was chosen for experiments to maximize the light penetration depth in tissues.

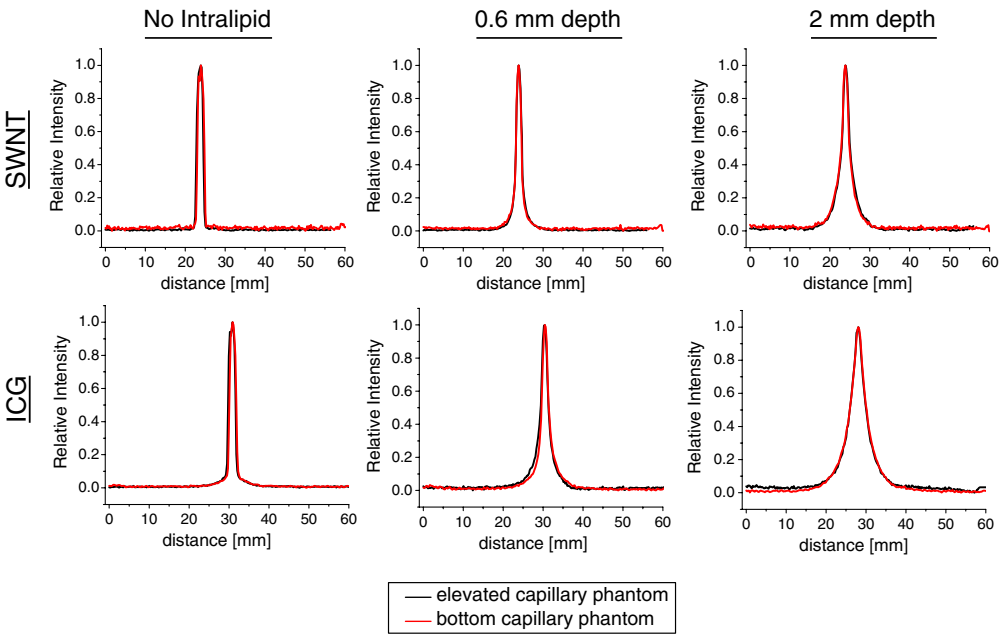

Fig. S11. Capillary phantom setup. To rule out signal alterations from the bottom of the dish during phantom tests, measurements were done in two geometries. The first geometry placed the capillary tube on the bottom of a glass dish, whereas the second elevated the capillary approximately 1.8 cm above the bottom of the dish. Both phantom geometries were imaged at multiple Intralipid® depths as described in the *Methods* section of the main text. Line cuts of both indocyanine green (ICG) and SWNT capillary images show that there is no difference in the signal scattering due to phantom geometry.

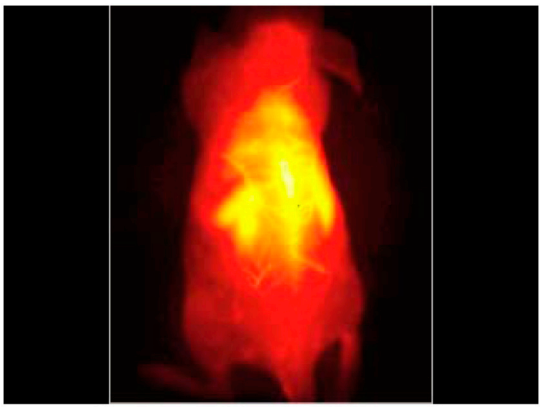

Movie S1. Video of intravenous injection—back view. View of the back of a mouse during tail-vein injection of SWNTs. The head of the animal is located at the top of the screen. The video frame rate is 14 frames per second.
Movie S1 (MOV)

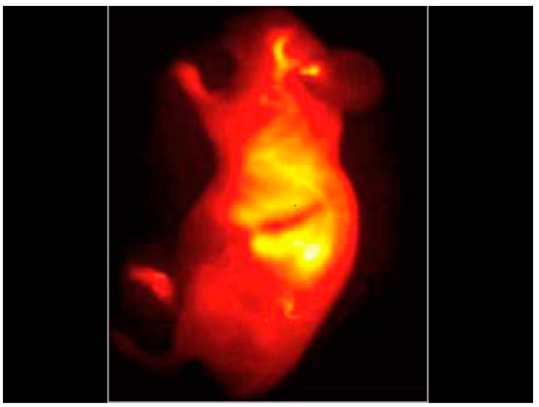

Movie S2. Video of intravenous injection—side view. View of the left side of a mouse during tail-vein injection of SWNTs. The head of the animal is located at the top of the screen. The video frame rate is 14 frames per second.
Movie S2 (MOV)

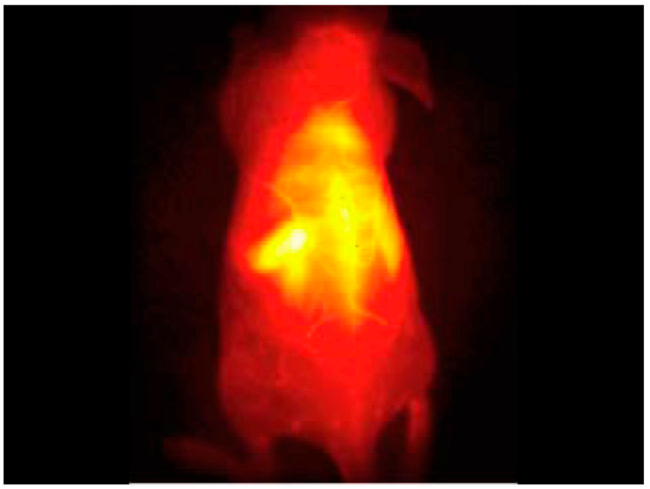

Movie S3. Video of intravenous injection—breathing removed. View of the back of a mouse during tail-vein injection of SWNTs. To remove major breathing movements that could affect PCA, frames where the animal is breathing have been removed. The head of the animal is located at the top of the screen. The video frame rate is 14 frames per second.
Movie S3 (MOV)